Supplementary Material for
"Revealing inherent quantum interference and entanglement of a Dirac Fermion"

Wen Ning,[1,*] Ri-Hua Zheng,[1,*] Yan Xia,[1] Kai Xu,[2,3] Hekang Li,[2] Dongning Zheng,[2,3] Heng Fan,[2,3] Fan Wu,[1,†] Zhen-Biao Yang,[1,‡] and Shi-Biao Zheng[1,§]

[1] *Fujian Key Laboratory of Quantum Information and Quantum Optics, College of Physics and Information Engineering, Fuzhou University, Fuzhou, Fujian 350108, China*
[2] *Institute of Physics, Chinese Academy of Sciences, Beijing 100190, China*
[3] *CAS Center for Excellence in Topological Quantum Computation, University of Chinese Academy of Sciences, Beijing 100190, China*

CONTENTS

S1. SYNTHESIS OF THE DIRAC HAMILTONIAN

A. Theoretical model

To realize the spinor-momentum coupling, the excitation energy of the test qubit is periodically modulated as ($\hbar = 1$ hereafter)

$$\omega_q(t) = \omega_0 + \varepsilon_1 \cos(\nu_1 t) + \varepsilon_2 \cos(\nu_2 t), \tag{S1}$$

where ω_0 is the mean excitation energy, and ε_j and ν_j ($j = 1, 2$) are the corresponding modulation amplitude and angular frequency, respectively. In addition to interaction with the resonator, the qubit is driven by a continuous microwave with frequency ω_0. The system Hamiltonian is given by

$$H = H_0 + H_I, \tag{S2}$$

* These authors contribute equally to this work.
† t21060@fzu.edu.cn
‡ zbyang@fzu.edu.cn
§ t96034@fzu.edu.cn

where

$$H_0 = \omega_r a^\dagger a + [\omega_0 + \varepsilon_1 \cos(\nu_1 t)] |e\rangle \langle e| ,$$
$$H_I = \varepsilon_2 \cos(\nu_2 t) |e\rangle \langle e| + (-\lambda a^\dagger |g\rangle \langle e| + \Omega e^{i\theta} e^{i\omega_0 t} |g\rangle \langle e| + \text{H.c.}), \tag{S3}$$

λ is the qubit-resonator coupling strength, and Ω (θ) denotes the amplitude (phase) of the classical driving field. We here assume $\omega_r = \omega_0 + 2\nu_1$. With this setting, the resonator interacts with the qubit at the second sideband associated with the first modulation, while the microwave drive works at the carrier. Performing the transformation

$$U_0 = \exp\left(i \int_0^t H_0 \ \mathrm{d}t\right), \tag{S4}$$

we obtain the system Hamiltonian in the interaction picture

$$H_I' = \varepsilon_2 \cos(\nu_2 t) |e\rangle \langle e| + \exp\left[-i\mu \sin(\nu_1 t)\right] \left[-\lambda \exp\left(2i\nu_1 t\right) a^\dagger + \Omega e^{i\theta}\right] |g\rangle\langle e| + \text{H.c.}, \tag{S5}$$

where $\mu = \varepsilon_1/\nu_1$. To clarify the underlying physics clearly, we use the Jacobi-Anger expansion

$$\exp\left[i\mu \sin\left(\nu_1 t\right)\right] = \sum_{o=-\infty}^{\infty} J_o(\mu) \exp\left(io\nu_1 t\right), \tag{S6}$$

with $J_o(\mu)$ being the oth Bessel function of the first kind, we obtain

$$H_I' = \varepsilon_2 \cos(\nu_2 t)|e\rangle\langle e| + \sum_{o=-\infty}^{\infty} J_o(\mu) \left\{-\lambda \exp[-i(o-2)\nu_1 t] a^\dagger + \Omega e^{i\theta} \exp\left(-io\nu_1 t\right)\right\} |g\rangle\langle e| + \text{H.c.}. \tag{S7}$$

For λ, $\Omega J_0(\mu) \ll \nu_1$, the qubit interacts with the resonator at the upper second-order sideband modulation with $o = 2$, and is driven at the carrier with $o = 0$. With the fast oscillating terms being discarded, H_I' reduces to

$$H_I' = K\sigma_\theta + \frac{1}{2}\varepsilon_2 \cos(\nu_2 t)\sigma_z - \eta e^{-i\theta} a^\dagger (\sigma_\theta - i\sigma_{\theta+\pi/2}) + \text{H.c.}, \tag{S8}$$

where $K = \Omega J_0(\mu)$, $\eta = \lambda J_2(\mu)/2$, $\sigma_\theta = e^{i\theta} |g\rangle \langle e| + e^{-i\theta} |e\rangle \langle g|$, and $\sigma_z = |e\rangle \langle e| - |g\rangle \langle g|$. With the assumption $\nu_2 = 2K \gg \eta$, $\varepsilon_2/2$ and under the further transformation $\exp(iK\sigma_\theta t)$, the system Hamiltonian can be well approximated by

$$H_I'' = -\eta e^{-i\theta} a^\dagger \sigma_\theta + \text{H.c.} + \omega\sigma_\mathrm{z}, \tag{S9}$$

where $\omega = \varepsilon_2/4$. When $\theta = \pi/2$, this effective Hamiltonian has the same form as the 1+1 Dirac equation of a spin-1/2 particle, with the correspondence $c^* = \sqrt{2}\eta$ and $m^* c^{*2} = \omega$. Herein c^* and m^* denote the effective light speed and mass of the Dirac particle in the simulation, respectively.

B. System parameters

The whole electronics and wiring of the used superconducting 5-qubit sample [S1, S2] are shown in Fig. S1. Each frequency-tunable Xmon qubit has an individual flux line for its dynamic tuning and a microwave drive for controllably flipping its states. All the qubits are capacitively coupled to a bus resonator with coupling strength $\lambda_j \approx 2\pi \times 20$ MHz ($j = 1, 2$) and every qubit has a readout resonator for reading out its states. The bus resonator R is a superconducting coplanar waveguide resonator with fixed frequency $\omega_r/(2\pi) = 5.5835$ GHz, which is measured when all used qubits stay in ground states at their respective idle frequencies (See below, unused qubits are always at their sweet points ~ 6 GHz). More detailed parameters of the sample are listed in Tab. S1.

In this experiment, we use two qubits (Q_1, Q_2) and the bus resonator (R). One qubit (Q_1) is used to realize the effective Dirac model, and the other qubit (Q_2) is used to measure the photon number distribution of the bus resonator by resonant population exchange (see Sec. S4 A for details). For initialization, we wait for 300 μs to make sure all qubits return to their ground states, and then bias them to their idle frequencies, where single qubit gates and qubit states measurements are performed.

We use two independent XY signal channels controlled by Digital-to-Analog converters (DACs), to generate two microwave sequences. These two low-frequency microwave sequences are mixed with a continuous microwave by the In-phase and Quadrature (IQ) mixer to generate two tone pulses. This continuous microwave is a carrier microwave emitted by the microwave source (MS) and has a frequency of 5.21 GHz. One-tone pulse is used to drive the test

	$\omega_{10}/(2\pi)$ (GHz)	T_1 (μs)	T_2^* (μs)	T_2^{SE} (μs)	$\lambda/(2\pi)$ (MHz)	$\alpha/(2\pi)$ (MHz)	$\omega_{ro}/(2\pi)$ (GHz)	F_g	F_e
Q_1	5.260	21.5	1.1	6.0	19.91	250	6.764	0.983	0.937
Q_2	5.110	17.2	1.5	14.3	20.92	238	6.655	0.990	0.920
R	5.5835	12.9	234.5	-	-	-	-	-	-

TABLE S1. **Qubit and resonator characteristics.** The test qubit, auxiliary qubit, and bus resonator are denoted by Q_1, Q_2, and R, respectively. The idle frequencies of Q_j ($j = 1, 2$) are marked by $\omega_{10}/(2\pi)$, where the pulses for initial state preparation and tomographic pulses for qubit measurement are applied. The energy relaxation time, the Ramsey Gaussian dephasing time, and the spin echo Gaussian dephasing time are T_1, T_2^* and T_2^{SE}, respectively, all measured at the idle frequency of each qubit. The coupling strength λ_j between the qubits Q_j and bus resonator R is measured by their population exchange rate at resonance. The symbol α is the anharmonicity of the qubits, ω_{ro} is the bare frequency of qubit's readout resonator, and F_g (F_e) is the probability of reading out Q_j in $|g\rangle$ ($|e\rangle$) when it is prepared in $|g\rangle$ ($|e\rangle$).

qubit to prepare the initial states, the other is used to trigger the resonator by crosstalk instead of the resonator line to achieve the displacement operation on its states in phase space, and to provide continuous driving pulses for Klein tunneling. For the Z signal, we use two independent channels on the DACs to control, which allows us to flexibly adjust the qubit frequency. In addition to the DACs described above, we need XY signal from the DACs to output the readout pulse with multiple tones implemented by sideband mixing. Then, the output pulse passes through the circulator, impedance-transformed Josephson parametric amplifier (JPA), cryogenic amplifier, and room temperature amplifier to improve signal-to-noise ratio. Finally, it is captured by Analog-to-Digital converters (ADCs) after passing through the readout resonator, and thus the multiple tones are demodulated to return the IQ information of each tone. The readout of the qubit states is performed at its idle frequency with the duration time of 1 μs. Both DACs and ADCs are supplied with the carrier microwave from the same MS. The frequency of the readout resonator $\omega_{ro}/(2\pi)$ ranges from 6.65 to 6.86 GHz, right in the bandwidth of our JPA with a pump frequency about 13.39 GHz.

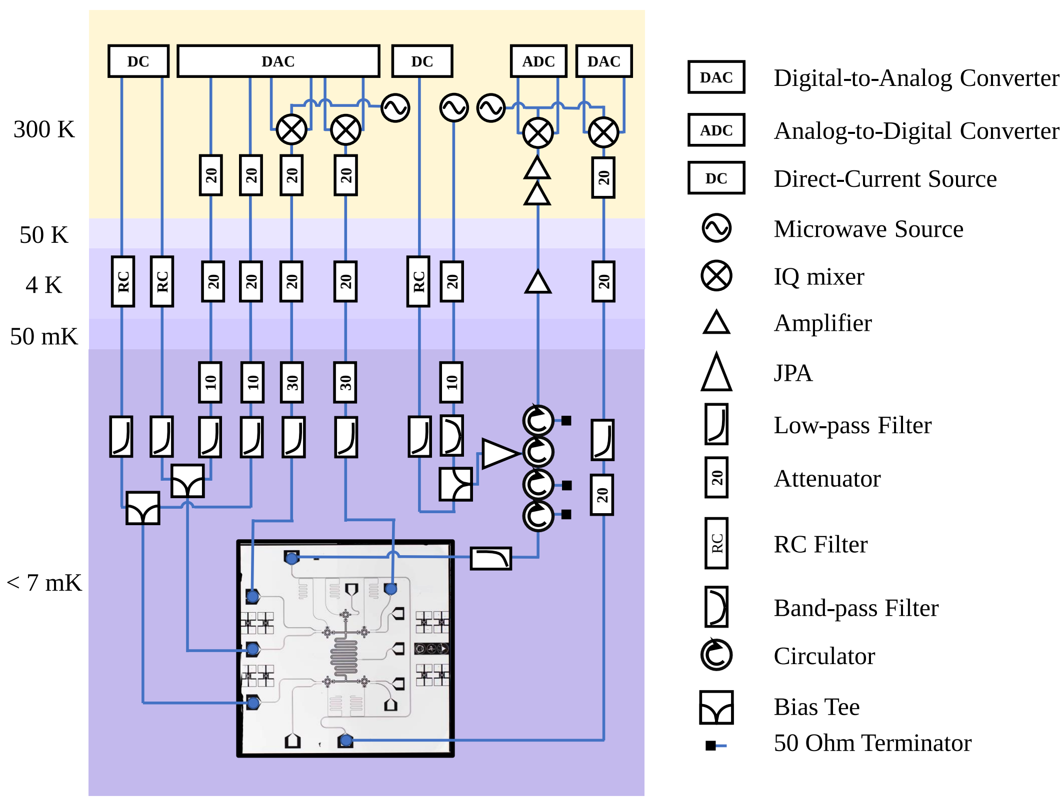

FIG. S1. **Schematic diagram of the experimental setup.** Note there is a low-pass filter inverted with the others because it connects to the readout line. The number inside the attenuator icon indicates the magnitude of the attenuator in dBm.

During the procedure of qubit's initial state preparation and measurement, some errors are caused by decoherence.

To calibrate these errors, we use a calibration matrix, defined as

$$F_j = \begin{pmatrix} F_{g,j} & 1 - F_{e,j} \\ 1 - F_{g,j} & F_{e,j} \end{pmatrix}, \tag{S10}$$

where $F_{g,j}$ and $F_{e,j}$ are the readout fidelities of qubits Q_j (see Tab. S1), to reconstruct the readout results. Defining $F = F_1 \otimes F_2$ as a two-qubit calibration matrix. We rewrite the measurement results of two qubits into a column vector P_m, and the calibrated measurement result is then $P = F^{-1} \cdot P_m$.

S2. NUMERICAL SIMULATIONS OF PHASE-SPACE QUANTUM INTERFERENCE

A. Interference between Positive and Negative Components

To further confirm the experimental results indeed reflect the quantum dynamics of Dirac Fermions, we perform numerical simulations based on the ideal Dirac Hamiltonian. The resonator WFs correlated with the qubit's $|g\rangle$ and $|e\rangle$ states after 330 ns are respectively shown in Figs. S2(a) and S2(b), while the result irrespective of the qubit state is displayed in Fig. S2(c). In the numerical simulations, the Hamiltonian parameters and the system initial state are the same as those for the experimental simulations displayed in Fig. 2 of the main text. The numerical results with the full Hamiltonian are displayed in Fig. S3. To compensate for the difference due to the Stark shifts produced by the discarded off-resonant couplings, we perform proper phase-space rotations, which, however, do not change the quantum effects in any way. The numerical simulations of the evolutions of the mean position $\langle x \rangle$ and entropy are displayed in Fig. S4. All these numerical results agree well with the experimental simulations shown in Fig. 2 of the main text.

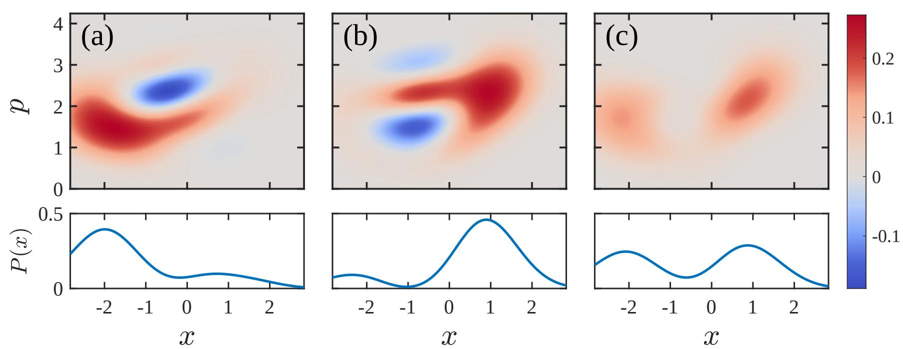

FIG. S2. **Numerical simulations of phase-space quantum interference, governed by the effective Hamiltonian Eq. (S9).** (a), (b) WFs correlated with the basis states $|g\rangle$ and $|e\rangle$ of the test qubit; (c) WFs irrespective of the test qubit's state, all obtained after an evolution time of 330 ns. Lower panels: Probability distributions $P(x)$ with respect to the quadrature x, obtained by integrating the corresponding WFs over p.

B. Interference between Positive Components with Different Momentums

As stated in the main text, quantum interference is actually a universal inherent characteristic of Dirac Fermions, which can manifest itself even without negative components. When the initial state is restricted to the positive branch, the system state can be written as

$$|\psi_+(t)\rangle = \int \mathrm{d}p \; e^{-iE_p t} \xi_p |p\rangle |\phi_+(p)\rangle. \tag{S11}$$

We assume that $|\xi_p|^2$ satisfies Gaussian distribution, i.e., $|\xi_p|^2 = 1/(\delta p\sqrt{2\pi})e^{-(p-p_0)^2/(2\delta p^2)}$, with $p_0 = 1$, $\delta p = 1$. To demonstrate the phase-space quantum interference, we project the system state along the basis $\{|B_\pm\rangle\} = \{|e\rangle, |g\rangle\}$ and deduce the WF signal, given by

$$\mathcal{W}_\pm(x,p,t) = \frac{1}{\pi}\int \mathrm{d}v \; \varphi_\pm^*(p+v)\varphi_\pm(p-v)e^{-2ivx}, \tag{S12}$$

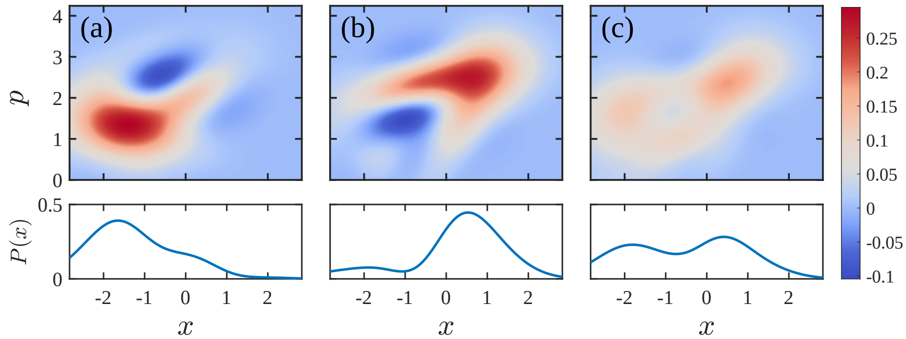

FIG. S3. **Numerical simulations of phase-space quantum interference, governed by the full Hamiltonian Eq. (S2).** (a), (b) WFs correlated with the basis states $|g\rangle$ and $|e\rangle$ of the test qubit; (c) WFs irrespective of the test qubit's state, all deduced after an evolution time of 330 ns. Lower panels: Probability distributions $P(x)$ with respect to the quadrature x, obtained by integrating the corresponding WFs over p.

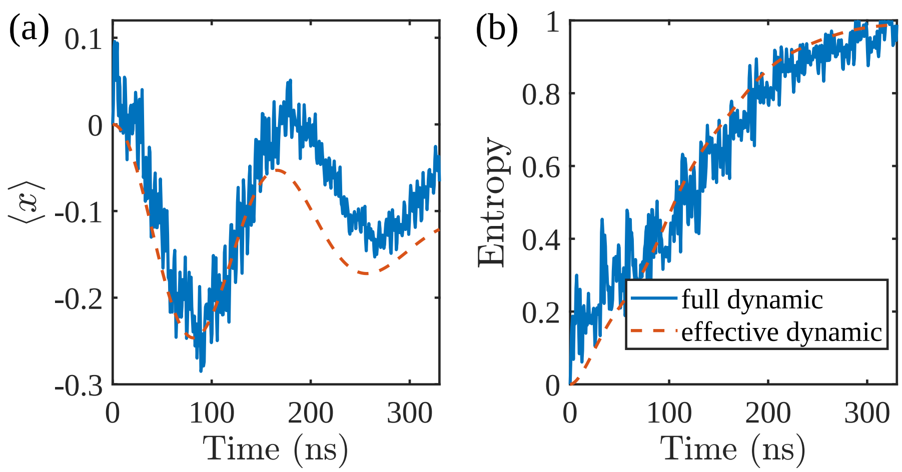

FIG. S4. **Numerical simulation of *Zitterbewegung*.** (a) Mean position $\langle x\rangle$ versus time. (b) Entropy versus time. The solid and dashed lines represent the results of full and effective dynamics (governed by full and effective Hamiltonians), respectively.

where $\varphi_{\pm}(p) = \xi_p^* e^{-iE_p t}\langle B_{\pm}|\phi_+(p)\rangle$. Numerical simulations of such WFs are shown in Fig. S5, where we can see phase-space quantum interference patterns for different evolution times. The simulations are performed based on the ideal Dirac Hamiltonian with $m = 1$, and by setting $\hbar = c = 1$. An unexpected result is that the WFs, obtained irrespective of the internal state, also displays a time-evolving quantum interference pattern. This result is in distinct contrast with the case that the system is initially in the superposition of positive and negative components, for which the WFs exhibit a quantum interference pattern that appears only when correlating to the internal state. Such an unconditional feature further confirms the universality of the phase-space quantum interference behavior.

Based on Eq. (S11), the entropy is calculated by

$$S' = -\log_2\left(\int \mathrm{d}p\ |\xi_p|^2 |\phi_+(p)\rangle\langle\phi_+(p)|\right), \tag{S13}$$

The numerical result is presented in Fig. S6(a), which confirms that the internal and spatial freedom degrees remain highly correlated with a time-independent entanglement entropy. Additionally, the corresponding mean position $\langle x\rangle$ versus time is shown in Fig. S6(b), which exhibits a linear increase without *ZB*. These results unambiguously demonstrate that the Dirac particle evolves with a time-dependent quantum interference pattern, which is hidden in the entangled internal-spatial state, and expresses itself in the position-momentum quasiprobability distribution, correlated to the internal state.

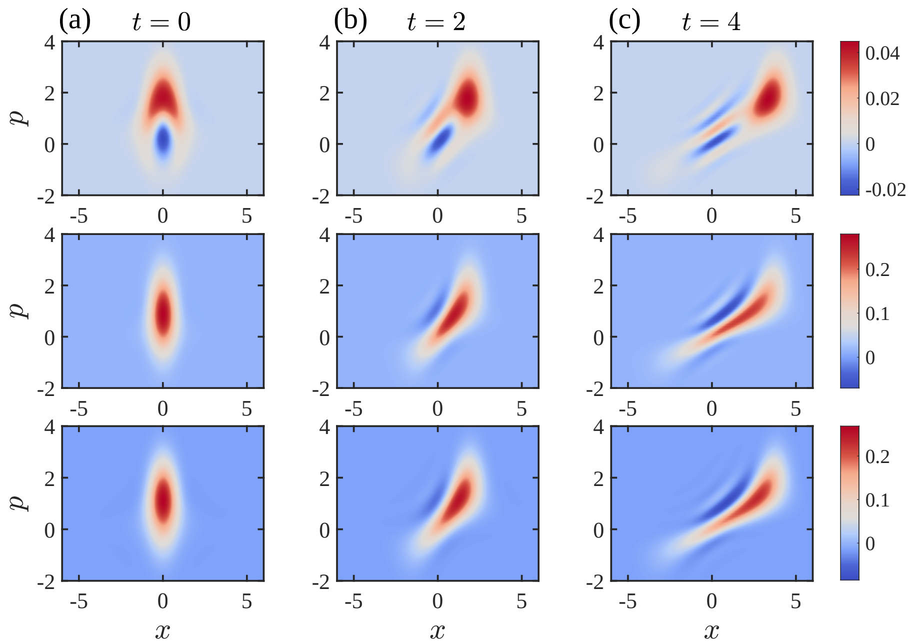

FIG. S5. **Time-evolving WFs associated with the positive branch.** The upper and middle rows respectively denote the WFs correlated with the internal states $|g\rangle$ and $|e\rangle$, and the lower row shows the results irrespective of the internal state. The momentum is supposed to have a Gaussian distribution, centered at $p_0 = 1$ with the spread $\delta p = 1$. The simulated Dirac particle has a mass of $m = 1$. The results for $t = 0$, 2, and 4 are shown in (a), (b), and (c), respectively. For simplicity, $\hbar$ and c in the Dirac Hamiltonian are both set to be 1.

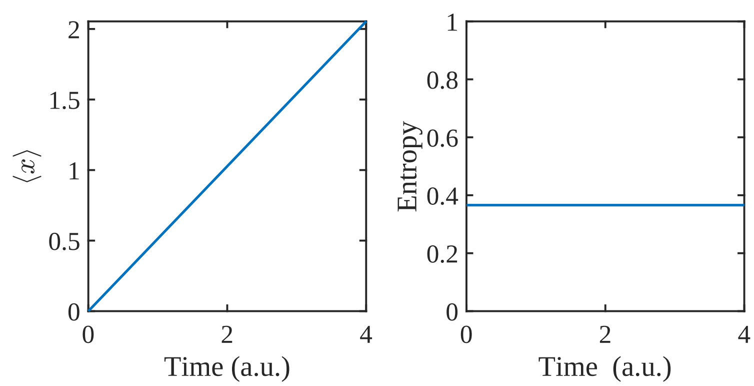

FIG. S6. **Entanglement entropy evolution and spatial motion for the positive branch.** The mean position $\langle x \rangle$ is calculated by integrating $x\mathcal{W}(x, p, t)$ over phase space.

S3. OPTIMIZATION OF DRIVING PULSES

A. Optimized Qubit Driving

To achieve a periodic modulation of the qubit frequency, we first measure the resonant frequency ω_{10} versus the Z-line pulse amplitude (ZPA) for the test qubit, the results are shown in Fig. S7 [S3]. Here we set the detuning between the idle frequency of the Q_1 and the resonator frequency being $\Delta/(2\pi) \approx 320$ MHz, and the frequency of the first modulation pulse $\nu_1/(2\pi) = 160$ MHz. In such a case, the working frequency of the qubit is the idle frequency point, avoiding a large rising edge at the beginning of the pulse. Considering the frequency of the second frequency modulation pulse $\nu_2/(2\pi) = 33.4$ MHz, this parameter setting will effectively reduce the high-energy level excitation caused by the modulation pulse. Subsequently, we modulate the qubit in the frequency with amplitude $\varepsilon_1 = 2\pi \times 130$ MHz, centering around its idle frequency according to the ω_q versus ZPA curves obtained previously.

Considering that the nonlinear curve of frequency versus ZPA and the limited DACs bandwidth lead to imperfect waveforms of the periodically modulated excitation energy, we modify the frequency-modulated pulse as

$$\omega_q(t) = \omega_0 + \delta + \varepsilon_1 \cos(\nu_1 t + \phi_1) + \varepsilon_2 \cos(\nu_2 t + \phi_2), \tag{S14}$$

making the experiment dynamics closer to the Dirac dynamics. We traverse these two phases (ϕ_1, ϕ_2) between 0 and 2π, set the initial state of the system to be $|\psi\rangle = \frac{1}{\sqrt{2}}(|e\rangle + |g\rangle) \otimes |0\rangle$ in both the ZB and Klein tunneling simulations, and finally obtain the one which is closest to the ideal situation. Here we use the 2-norm as an index to measure the agreement between the experimental population data of qubit state $|e\rangle$ and the theoretical values. Then, we optimize the δ and other parameters in the same way. In this case, the optimized population is shown in Fig. S8, and the experimental data are in good agreement with the ideal ones, which proves the correctness of our method.

For the transverse field driving the qubit, we want the microwave to arrive at the qubit with an initial phase $\pi/2$. Therefore, we use a similar approach to optimize this phase. In addition, in the application of modulated pulses, the oscillation center frequency of the qubit may deviate slightly from the working frequency ω_0, so we mildly tune the microwave frequency (about $1 \sim 2$ MHz) of the transverse field to make the results more predictable.

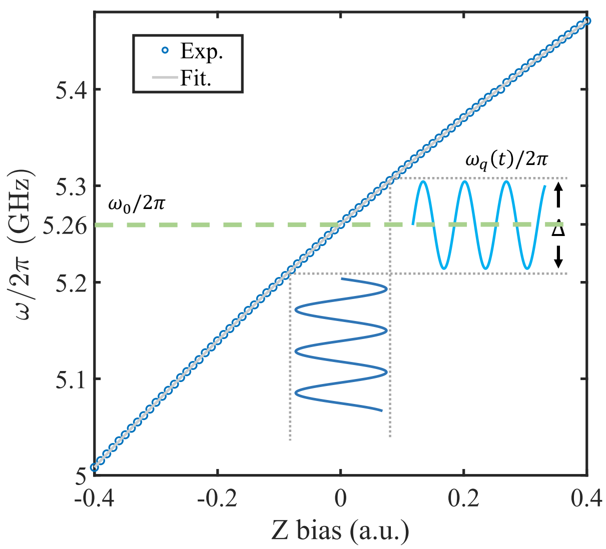

FIG. S7. **Frequence of the test qubit versus Z line bias.** The desired modulation of $\omega_q(t)$ can be realized by mapping it to the modulation of Z bias.

B. Optimized Bus Resonator Driving

The resonator is driven by using a flattop envelope with a resonance frequency, described as $\Omega_r(a + a^\dagger)$, where Ω_r is the Rabi frequency of the pulse. During the preparation of the initial state in the ZB simulation experiment, the presence of a dispersion coupling (form of $\sigma_z a^\dagger a$) between the test qubit and the bus resonator is $\lambda_1^2/\Delta \approx 2\pi \times 1.25$ MHz. So we reduce the pulse time and increase the Rabi frequency of the pulse to avoid the initial state rotation caused by the dispersion interaction. Lengths of pulse for initial state preparation and tomography pulse are 24 ns and 60 ns, respectively.

For pulses of a specific length, we apply them with different amplitudes to the resonator and measure the photon number to fit the slope between the Rabi frequency (Ω_r) and the pulse amplitude. Up to now, together with the initial phase of the microwave pulse, we can implement arbitrary displacement operators $D(\gamma)$ for Wigner measurements.

The Klein tunneling experiment requires a continuous pulse on the resonator during the dynamics. There is a fixed resonator frequency shift induced by the non-resonant coupling, thus we adjust the microwave frequency to about 0.75 MHz to get better results.

The qubit-state-dependent resonator frequency shift in the dynamical process is still unavoidable; therefore, additional correction of the results is necessary so as to make the results more intuitive (see Sec. S5).

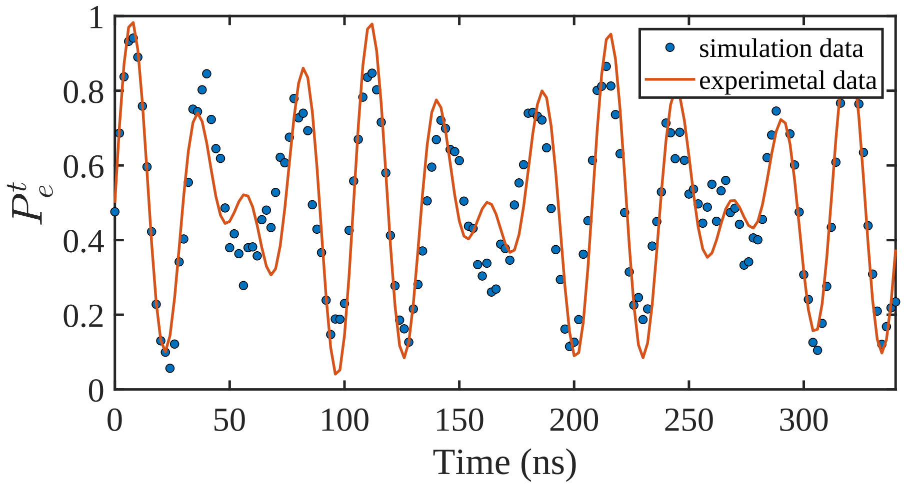

FIG. S8. **Validity check of the Rabi model.** For the present Rabi model, the effective frequency of the qubit and the effective coupling strength are $\omega/(2\pi) = 2.2$ MHz and $\eta = 2\pi\times$ 0.78 MHz, respectively. We fix the initial state as $|\psi_0\rangle = \frac{1}{\sqrt{2}}(|g\rangle+|e\rangle)\otimes|0\rangle$. After optimizing parameters ε_1, ε_2, ϕ_1, ϕ_2, and δ appropriately, in the experiment, we measure the population of the test qubit state $|e\rangle$, marked as P_e^t, at different times, and compare it with the numerical results.

C. Full Pulse Sequence

The pulse sequence is shown in Fig. S9, including three steps: 1. Initial state preparation; 2. Dirac dynamics; 3. Quantum state measurement. For clarity of reading, the real-time scales are not used in the figure.

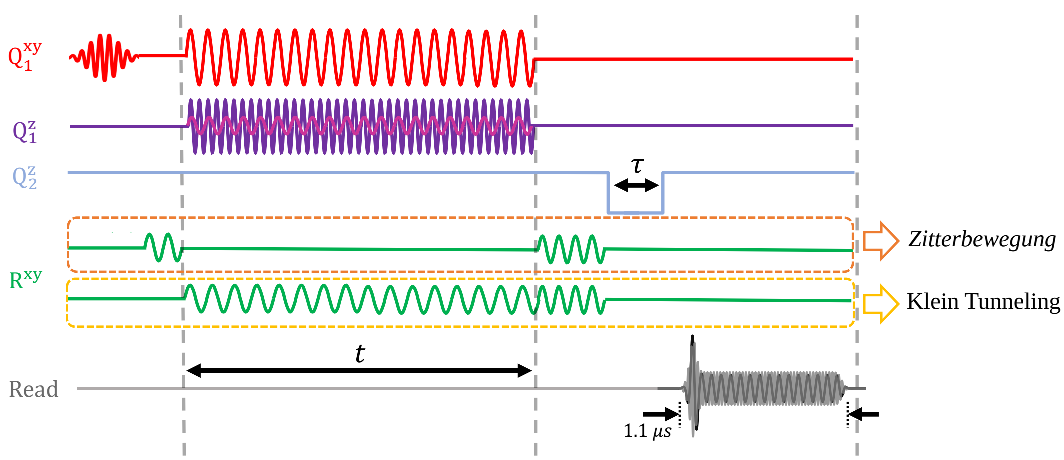

FIG. S9. **Sketch of the Pulse Sequences.** The test qubit Q_1 is driven by a transverse microwave field with the Rabi frequency $\Omega/(2\pi) \approx 20.03$ MHz through the XY-line (red), and two Sine longitudinal modulations apply to the Z-line (purple) with the modulation frequencies $\nu_{1(2)}/(2\pi) = 160$ (33.4) MHz and the amplitudes $\varepsilon_{1(2)} = 2\pi \times 130$ (8.8) MHz in the *ZB* simulation. While in the Klein tunneling simulation, we set $\varepsilon_2 = 0$ to simulate massless particles. The orange dashed box represents the pulse sequence of R^{xy} used in the *ZB* simulation, which is replaced by the series of yellow dashed boxes in the Klein tunneling simulation, and outside the dashed box there are the same pulse sequences for these two simulations. The evolution times t of the two experiments are 330 ns and 288 ns, respectively. The auxiliary qubit Q_2 is used to measure the resonator photon number. After the displacement operation pulse, we bias Q_2 to the resonator frequency for a given time τ and then deduce the photon number distribution of the resonator according to the result of the Rabi oscillation. Finally, a multiplexing tone is applied to the readin line to simultaneously measure two qubits' states.

S4. CHARACTERIZATION OF THE QUBIT-RESONATOR STATE

A. Photon-Number Distribution

All the WF values in the main text are deduced from the photon number distribution. We use the same method as in Ref. [S4]. After the Dirac dynamics and displacement operation, we bias the auxiliary qubit Q_2 to the frequency of the bus resonator for a given time τ. Then, we bias it to the idle frequency and measure. The excited state population $P_e^a(\tau)$ of Q_2 is defined as

$$P_e^a(\tau) = \frac{1}{2}\left[1 - P_g^a(0)\sum_{n=0}^{n_{\max}} P_n e^{-\kappa_n \tau}\cos\left(2\sqrt{n}\lambda_2\tau\right)\right], \tag{S15}$$

where P_n denotes the photon-number distribution probability, $n_{\max}$ is the cutoff of the photon number, and $\kappa_n = n^l/T_{1,p}$ $(l = 1)$ [S5–S9] is the empirical decay rate of the n-photon state, λ_2 is the coupling strength between auxiliary qubit Q_2 and resonator. It is worth noting that due to the finite detuning $\Delta = 2\pi \times 470$ MHz between the auxiliary qubit Q_2 and bus resonator R, as the number of photons increases, ancilla qubit Q_2 inevitably interacts with the resonator during the Dirac dynamics, the ground state population $P_g^a(0)$ may not be 1 at $\tau = 0$. Referring to [S5], the potentially slight excitation can be ignored and thus $P_g^a(0)$ is introduced to make the fit more accurate. In the experiment, $P_g^a(0) \leq 0.05$, τ is taken every 2 ns from 0 to 200 ns. We use the least square method to fit the experimental data according to Eq. (S15) to obtain the actual photon number distribution and further obtain the value of the WF. However, with the further increase of the photon number, the entanglement between the auxiliary qubit Q_2 and the resonator can not be ignored, and the photon number and its distribution in the resonator can not be obtained accurately. It is also worth noting that although ancilla qubits can be biased further down to increase the detuning in the Dirac dynamics, the performance of the qubits deteriorates and the frequency changes more widely, affecting the measurement results. Ergo, the photon number capability of the present system is about 20, resulting in the boundary of phase-space in the main text.

B. Wigner Matrix Elements

The WF is given by

$$\mathcal{W}(x,p) = \frac{1}{\pi}\sum_{n=0}^{\infty}(-1)^n \mathcal{P}_n(\gamma), \tag{S16}$$

$$\mathcal{P}_n(\gamma) = \langle n|\, D(-\gamma)\rho D(\gamma)\,|n\rangle\,, \tag{S17}$$

where $x = \sqrt{2}\mathrm{Re}(\gamma)$, $p = \sqrt{2}\mathrm{Im}(\gamma)$, $D(\gamma) = \exp\left(\gamma a^\dagger - \gamma^* a\right)$. The photon number distribution $\mathcal{P}_n$ is inferred by the Rabi oscillation signal [S9]. And then we calculate the Wigner matrix according to Eq. (S16). We adjust the Wigner tomography pulse based on γ to realize the measurement of WF values at different positions in phase-space. The WF conditional on test qubit states $|e\rangle$ and $|g\rangle$ are given by

$$\mathcal{W}_{e(g)}(x,p) = \frac{1}{\pi}\sum_{n=0}^{\infty}(-1)^n \mathcal{P}_n^{e(g)}(\gamma), \tag{S18}$$

$$\mathcal{P}_n^{e(g)}(\gamma) = \frac{1}{P_k^t}\langle n| \otimes \langle e(g)|\, D(-\gamma)\rho D(\gamma)\,|e(g)\rangle \otimes |n\rangle\,, \tag{S19}$$

with P_k^t being the population of the test qubit Q_1 in $|k\rangle$ state at time t.

In this way, we can get all the information about the resonator state. Then, we use the CVX toolbox based on MATLAB [S10] to reconstruct the corresponding density matrix ρ_k to calculate the average position $\langle x\rangle$ and average momentum $\langle p\rangle$ of the resonator.

As mentioned in the main text, a larger number of photons requires Wigner tomography within a larger phase-space region. Due to the hardware-limited pulse amplitude, we can increase the size of $|\gamma|$ by increasing the length of the tomography pulse, at the cost of increasing the dispersive interaction time. Considering the finite detuning between the auxiliary qubit and the resonator, our *ZB* simulation ends at 330 ns. With the improvement of the hardware, such as larger pulse amplitude, or better qubits performance, we could simulate the *ZB* behavior within a longer time scale.

S5. CORRECTION OF PHASE-SPACE ROTATIONS DUE TO STARK SHIFTS

After reconstructing the density matrix ρ_k from the Wigner tomography $\mathcal{W}_k$, we add a rotation operator on the corresponding density matrix numerically. The rotation operator is defined as

$$U_k = \exp\left[-i(\theta_{k,0} + \theta_k t/t_f)a^\dagger a\right], \tag{S20}$$

$$\rho'_k = U_k \rho_k U_k^\dagger, \qquad (k = e, g) \tag{S21}$$

where $\theta_{k,0}$ is used to counteract the resonator states rotation due to the initial state preparation when the test qubit in $|k\rangle$ state, θ_k cancels out the rotation caused by the difference between the experimental frame and the effective Hamiltonian frame in Eq. (S9), t_f is the end time of each simulation, and ρ'_k is the resonator density matrix after rotation when the test qubit in $|k\rangle$ state. In the Klein tunneling simulation experiment, because the initial state of the resonator is a vacuum state, we set $\theta_{k,0} = 0$. Here we choose $(\theta_{e,0}, \theta_{g,0}, \theta_e, \theta_g, t_f) = (0.260, 0.045, 1.510, 1.217, 330\text{ ns})$ in the *ZB* simulution and $(\theta_{e,0}, \theta_{g,0}, \theta_e, \theta_g, t_f) = (0, 0, 1.402, 1.162, 280\text{ ns})$ in the Klein tunneling simulation. Note θ_e and θ_g are slightly different because the dispersive interaction during Wigner tomography (time scale 60 ns, causing phase difference $2\lambda_1^2/\Delta \times 60\text{ ns} \sim 0.3$). While both θ_e and θ_g are around 1.3, offsetting the resonator phase induced by the frame difference, and therefore demonstrating that the rotation of our data is reasonable. The unconditional resonator WF is obtained by adding two rotated WFs according to the corresponding qubits state population:

$$\mathcal{W}'(t) = P_e^t \mathcal{W}'_e(t) + P_g^t \mathcal{W}'_g(t), \tag{S22}$$

where $\mathcal{W}'_k(t)$ is calculated from ρ'_k. The complete Wigner data are shown in Fig. S10 for *ZB* simulation and Fig. S11 for Klein tunneling simulation. For the selection of the time point, we try to make the population of states $|e\rangle$ and $|g\rangle$ of the test qubit close to 0.5, making the normalized data of the auxiliary qubit accurate and convenient to fit the photon number distribution of the resonator.

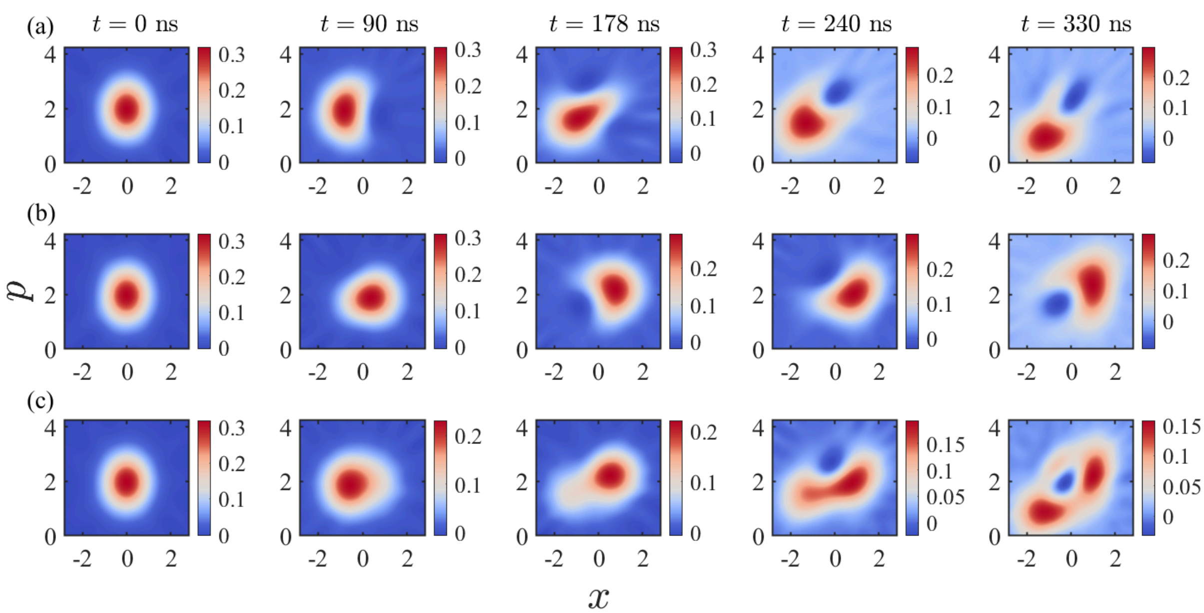

FIG. S10. **Wigner functions for *Zitterbewegung*.** The WFs correlated with the basis states $|g\rangle$ and $|e\rangle$ of the test qubit displayed in (a) and (b), respectively, and (c) show the result irrespective of the test qubit's state. These five columns show the WFs at different times: 0, 90, 178, 240, and 330 ns.

S6. DISCRIMINATION BETWEEN POSITIVE AND NEGATIVE COMPONENTS IN KLEIN TUNNELING

In the Klein tunneling simulation, we need to show the measured position average $\langle x\rangle$ and momentum average $\langle p\rangle$ for the positive and negative wavepackets. Here, we simply use $x = 0$ as a boundary to distinguish positive and

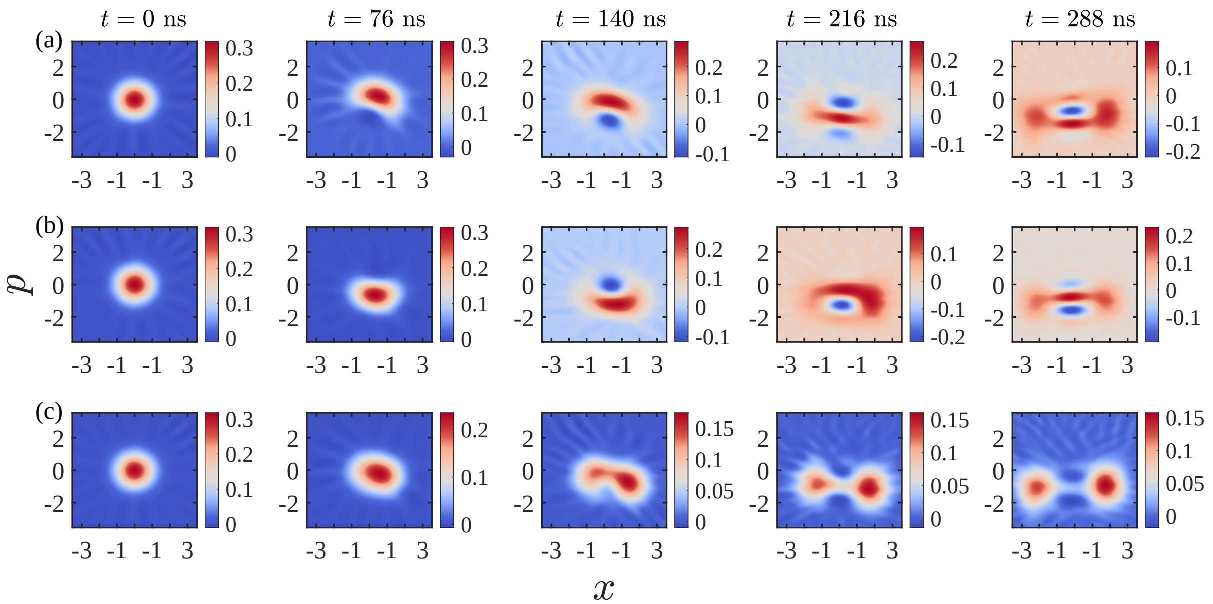

FIG. S11. **Wigner function for Klein tunneling.** The WFs correlated with the basis states $|g\rangle$ and $|e\rangle$ of the test qubit displayed in (a) and (b), respectively, and (c) show the result irrespective of the test qubit's state. These five columns show the WFs at different times: 0, 76, 140, 216, and 288 ns.

negative wavepackets. The measured $\langle x\rangle$ and $\langle p\rangle$ for positive wavepackets can be calculated by

$$\langle x\rangle = \frac{\int_{-\infty}^{+\infty}\int_{0}^{+\infty} x\mathcal{W}(x,p)\ \mathrm{d}x\mathrm{d}p}{\int_{-\infty}^{+\infty}\int_{0}^{+\infty} \mathcal{W}(x,p)\ \mathrm{d}x\mathrm{d}p}, \tag{S23}$$

$$\langle p\rangle = \frac{\int_{-\infty}^{+\infty}\int_{0}^{+\infty} p\mathcal{W}(x,p)\ \mathrm{d}x\mathrm{d}p}{\int_{-\infty}^{+\infty}\int_{0}^{+\infty} \mathcal{W}(x,p)\ \mathrm{d}x\mathrm{d}p}, \tag{S24}$$

where $\mathcal{W}(x,p)$ is shown in Fig. S11(c). At $t = 0$ and 76 ns, the positive and negative wavepackets cannot be fully distinguished, so the data for these two mean positions $\langle x\rangle$ are abandoned in Fig. 3(d) of the main text. The negative wavepacket can be obtained in the same way,

$$\langle x\rangle = \frac{\int_{-\infty}^{+\infty}\int_{-\infty}^{0} x\mathcal{W}(x,p)\ \mathrm{d}x\mathrm{d}p}{\int_{-\infty}^{+\infty}\int_{-\infty}^{0} \mathcal{W}(x,p)\ \mathrm{d}x\mathrm{d}p}, \tag{S25}$$

$$\langle p\rangle = \frac{\int_{-\infty}^{+\infty}\int_{-\infty}^{0} p\mathcal{W}(x,p)\ \mathrm{d}x\mathrm{d}p}{\int_{-\infty}^{+\infty}\int_{-\infty}^{0} \mathcal{W}(x,p)\ \mathrm{d}x\mathrm{d}p}. \tag{S26}$$

[S1] C. Song *et al.*, "Continuous-variable geometric phase and its manipulation for quantum computation in a superconducting circuit," *Nat. Commun.* **8**, 1061 (2017).
[S2] W. Ning *et al.*, "Deterministic entanglement swapping in a superconducting circuit," *Phys. Rev. Lett.* **123**, 060502 (2019).
[S3] W. Liu *et al.*, "Synthesizing three-body interaction of spin chirality with superconducting qubits," *Appl. Phys. Lett.* **116**, 114001 (2020).
[S4] R.-H. Zheng *et al.*, "Emergent Schrödinger cat states during superradiant phase transitions." arXiv:2207.05512 (2022)
[S5] M. Hofheinz *et al.*, "Synthesizing arbitrary quantum states in a superconducting resonator," *Nature* **459**, 546–549 (2009).
[S6] D. M. Meekhof, C. Monroe, B. E. King, W. M. Itano, D. J. Wineland, "Generation of nonclassical motional states of a trapped atom," *Phys. Rev. Lett.* **76**, 1796–1799 (1996).
[S7] D. Leibfried, R. Blatt, C. Monroe, D. Wineland, "Quantum dynamics of single trapped ions," *Rev. Mod. Phys.* **75**, 281–324 (2003).
[S8] D. Lv *et al.*, "Quantum simulation of the quantum Rabi model in a trapped ion," *Phys. Rev. X* **8**, 021027 (2018).

[S9] M.-L. Cai *et al.*, "Observation of a quantum phase transition in the quantum Rabi model with a single trapped ion," *Nat. Commun.* **12**, 1126 (2021).

[S10] M. Grant, S. Boyd, CVX: Matlab software for disciplined convex programming, version 2.0 beta. http://cvxr.com/cvx, September (2013).